UNIVERSITY
OF TURKU

Optimizing Solar Power Plant Efficiency: Advancements in Hot Area Cooling Systems

Materials Engineering of Energy and Technology
Department of Mechanical and Materials Engineering
Faculty of Technology
Master's thesis

Author:
Ana Laura Mariscal Gonzalez

July 2025
Turku

Master's thesis

Subject: Materials Engineering
Author: Ana Laura Mariscal Gonzalez
Title: Optimizing Solar Power Plant Efficiency: Advancements in Hot Area Cooling Systems
Supervisor(s): Dr Aapo Poskela & Managing Director Henri Nieminen (Finnfoam Oy)
Number of pages: -thesis, 53 pp., 4 appendices.
Date: June 2025

Solar energy has become a widely adopted and sustainable alternative for power generation. However, solar panels, present performance limitations such as the decrease on performance when its working temperature exceeds 25°C [1]. This issue is especially pronounced in regions near the equator, where high solar exposure that leads to more energy production, is accompanied by elevated ambient temperatures that cause thermal stress on Photovoltaic (PV) systems and reducing their overall effectiveness. This study addresses the performance limitations of solar panels in hot climates by evaluating an active cooling system designed to reduce panel temperatures and improve efficiency. A three-year experimental analysis (2022–2024) was conducted in Southwest Finland on three solar panel arrays. In the final year, a cooling system—comprising a network of coolant-carrying pipes—was installed under one array, and its performance was compared across the summer months (July–September) of each year. Additionally, a computational model replicating the cooling setup was developed, incorporating variables such as geographic location, solar position, irradiation, and ambient temperature. The model was further applied to simulate conditions in the Tabernas Desert in Spain to assess its effectiveness in hotter climates. It also explored system optimization by adjusting design parameters and environmental inputs, offering a versatile tool for adapting cooling systems to various geographical settings.

Keywords: Solar panel, active cooling, computational model.

Acknowledgments

I would like to express my sincere gratitude to Finnfoam Oy for the opportunity to work on this project. I am also deeply thankful to my family and friends for their unwavering support and encouragement throughout this journey. Additionally, I acknowledge the use of generative AI language models to assist with grammar, spelling, and style refinement.

Contents

List of Abbreviations

Abbreviation	Full Term
ADRASE	Acceso a Datos de Radiación Solar de España
c-Si	Crystalline silicon
DC	Direct current
EVA	Ethylene-vinyl acetate
GHI	General horizontal solar irradiation
PE	Polyethylene
PEX	Cross-linked polyethylene
PV	Photovoltaic
PVC	Polyvinyl chloride
PVGIS	Photovoltaic Geographical Information System
PV/T	Photovoltaic thermal

1 Introduction

Global energy consumption demands increase annually [2]. To meet this demand in an environmentally sustainable manner, alternative sources considered clean and renewable, such as solar energy are proving to be exceptionally promising. Especially in equatorial regions, long daylight hours and consistent solar irradiance year-round are prime locations for solar cell energy encapsulation. However, in 2023, only 2.4 percent of the total energy generated in the world came from solar sources[2].

To illustrate the theoretical potential of solar energy, the Sahara Desert serves as a compelling example. Estimates suggest that covering just 1.3% of its total area (9.2 million km^2) with solar panels could generate enough electricity to meet the entire world's daily energy consumption [3]. Thanks to its proximity to the equator, the desert benefits from consistent solar exposure throughout the year, allowing photovoltaic (PV) panels to be installed at minimal tilt angles to maximize irradiation. In addition, much of the Sahara is inhospitable for agriculture or habitation, making it a practical location for large-scale solar installations without competing or impacting other land uses.

Despite the significant potential of solar farms in these regions, the reduction in efficiency caused by overheating of the panels must be considered. During sunny conditions, PV panel temperatures can reach as high as 70°C. The power output declines when working temperatures exceed 25°C. As a concrete example, in silicon cells the decay in the open circuit voltage (V_{OC}) is of about 0.4% per degree Celsius [4]. Moreover, the continuous operation in temperatures above 45°C represent a risk to the solar cells lifetime[1]. This thesis reviews various PV panel cooling systems and associated optimizations, which aim to lower operating temperatures and thereby recover efficiency in these technologies.

Finnfoam Oy has patented an active cooling system for solar panels, more specifically, a photovoltaic thermal (PV/T) collector that facilitates the intermittent circulation of a coolant solution through a piping system which alternates depth between the solar panels placed at ground level and deep ground as shown in Figure 1. The coolant collects excess heat from the solar panels and then runs deeper into the ground to dissipate this heat. The motivation for this project is to develop a cost-effective cooling system suitable for desert regions, where solar farms can be allocated with minimal impact in the large need of land for installation.

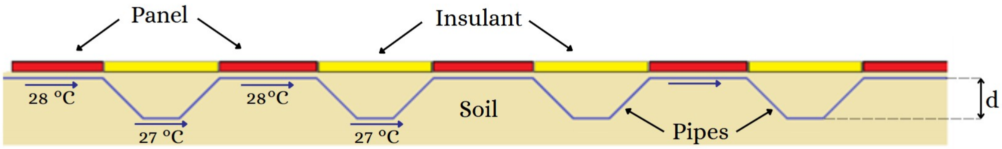

Figure 1: Representation of the PV/T system that collects excess heat from ground-level panels and dissipates it deeper into deep ground.

This thesis begins by presenting background information on the composition and operating principles of solar panels, which supports the rationale behind the decisions made throughout the project -particularly, the development of the computational model. It also includes a general overview of cooling systems for PV technologies and a description of the relevant methods in this work.The experimental setup is then described, focusing on an active cooling system designed by Finnfoam, along with two comparison configurations: a group of solar panels equipped with a passive air-based cooling system and a control group without any cooling feature. The thesis continues with a detailed explanation of how the computational model for the active cooling system was developed, validated, and applied to various case studies. Next, the results section provides a statistical analysis of the physical system layout and then transitions into the computational findings from the simulation, concluding with insights into potential system optimizations and a discussion of the results.

1.1 Solar panels

1.1.1 Composition

A typical crystalline silicon (c-Si) solar panel is composed of several key layers and components: the frame, front glass, encapsulant layers, solar cells, backsheet, and a junction box [5] illustrated in Figure 2.

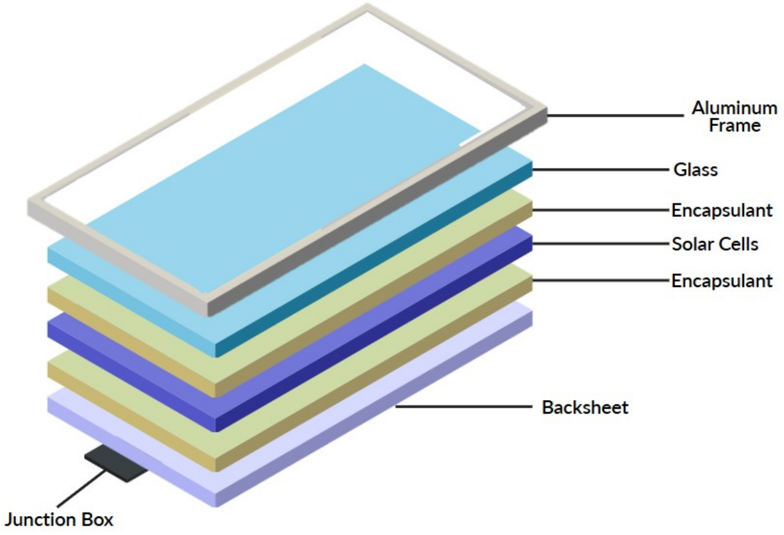

Figure 2: Structure of a PV module.

The front layer is usually made of tempered glass, which accounts for approximately 75% of the panel's weight [6]. This glass protects the solar cells from environmental conditions such as wind, snow, and rain. The solar cells themselves are the core components responsible for converting sunlight into electricity. Surrounding the cells are encapsulant layers—usually made of ethylene-vinyl acetate (EVA)—which act as strong, transparent adhesives applied under high heat (~ 150 °C). These layers also provide electrical insulation and structural cohesion. The panel is enclosed in an aluminum frame, which offers structural support but also adds significant weight. The backsheet, commonly made from durable fluoropolymers like Tedlar, insulates the panel and shields it from environmental damage. Finally, the junction box, located on the back of the panel, enables the collection and transfer of electricity while minimizing power losses due to partial shading [5].

1.1.2 Solar cell working principle

Inside the panel, solar cells are responsible for converting photon energy into direct current (DC) electricity through a chemical/physical phenomenon known as the photovoltaic effect. When sunlight is absorbed by the semiconductor material, it excites its electrons, promoting them from their ground state to a higher energy level. This excitation causes the separation of electrons from their atoms, creating free negative and positive charge carriers (electrons and holes). To generate usable current, these charges must be redirected to different terminals-electrons toward the cathode and holes toward the anode-. The electrons travel through an external circuit, where they lose energy in the form of electrical energy before recombining with the holes at the other terminal, completing the electrical cycle and returning the material to its ground state[7].

A key factor in this process is the band gap—the energy difference between the valence band (where electrons reside at rest) and the conduction band (where electrons are free to move and conduct electricity). For a photon to generate a charge carrier pair, its energy must be equal to or greater than the band gap of the semiconductor. If the photon energy is too low, it passes through the material without interaction; if it's too high, the excess energy is lost as heat. Thus, the band gap determines the range of sunlight energies that can be effectively converted to electricity [8].

As the temperature of the solar panel increases, the band gap of the solar cell semiconductor material narrows, leading to an increase in excited electrons. However, the excess of excited electrons that might look beneficial also results in an increased energy loss, which is dissipated as heat instead of electrical current. Consequently, the panel is heated not only by the ambient temperature but also by the internal heat resulting from its operation. This phenomenon significantly affects efficiency, as the panel's voltage is inversely related to temperature, resulting in reduced efficiency at higher operating temperatures [9].

1.2 Cooling systems

Commercial PV modules convert 6-20% of incident solar radiation into electricity, depending on the model and environmental conditions. The remaining absorbed radiation is converted into heat, elevating the temperature of the solar panels [10], [11]. Both module efficiency and power output present a linear dependency on operating temperature [10].This temperature-related performance variation is quantified by the temperature coefficient, which varies significantly depending on the materials used in the solar panel, generally in ranges of 0.2-0.5% per degree Celsius [1] [12] [13].

Cooling systems for PV technology are classified into passive and active techniques. Active cooling requires the circulation of a coolant (e.g., water, glycol, or air) using an external force, typically a pump. These methods are commonly capable to operate in relatively low temperatures with the use of refrigerant solutions with low or zero environmental impact. However, the operation of such systems, particularly pumps, implies energy consumption, which must be considered as an economic factor. [1], [14].

Passive techniques can be sub-classified into air-based methods (e.g., the elevation of panels on metallic structures to promote natural convection), water-based cooling (e.g., submersion), and thermal load reduction strategies (e.g., blocking a percentage of incoming solar radiation). Passive systems may also incorporate components such as heat pipes or heat exchangers to enhance heat dissipation. Due to their simplicity and lower operational demands, passive temperature reduction techniques are often considered cost-effective for energy production [1], [14]. This study analyzes a passive and active cooling technique based on the Finnfoam experimental layout, which will be detailed in the following sections.

1.2.1 Passive cooling through air

Air-based cooling techniques are characterized by their simplicity of design and absence of mechanical effort, factors that contribute to their popularity among various cooling methods. This technique is widely implemented in solar power plants [1].

Typically, these installations feature numerous solar panels or PV modules aligned in symmetrical rows and columns. The panels are strategically angled towards the sun for optimal sunlight absorption and are mounted on metal frames and foundations. This elevated mounting structure facilitates passive air cooling by allowing natural airflow around the panels. However, these support structures can significantly increase the overall costs associated with PV technologies[15].

1.2.2 Liquid-based cooling by forced water circulation

This sub method requires an external power source to pump a coolant through a network of pipes. The coolant absorbs heat from the solar panels primarily through convection. Notably, the coolant flow can create a temperature gradient along the panel, causing an uneven variation of temperature typically rising in the direction of the flow, potentially affecting the overall effectiveness of power production. The thermal behavior of the system involves heat transfer through conduction, convection, and radiation [16].

1.3 COMSOL Multiphysics

The project's experimental work involves creating a computational model using COMSOL Multiphysics, a simulation software package capable of constructing 3D geometries and applying multiphysics analyses. The primary COMSOL modules utilized are Fluid Dynamics, Heat Transfer, Pipe Flow, and the Materials Library. This simulation, along with all of its constituent components, will be described in detail in subsequent sections.

2 Description of the project

2.1 Physical experiment: Finnfoam Layout

The experimental layout is comprised of three groups (A, B, and C) each consisting of a single row of five solar panels, as shown in Figure 3. The groups A and B were placed at ground level on a sandy soil bed. The borders of these panel rows were surrounded by a thin layer of foam to minimize thermal exchange with the surroundings. In contrast, Group C was elevated above the ground on metal structures. All panels were oriented with an azimuth angle of 130° and a shallow tilt angle of 3°, primarily to facilitate rainwater runoff.

The system A served as the control group, being placed on the ground surface without additional cooling modifications during the entire testing period. Group B incorporated a pipe arrangement (detailed later in this section) through which a water-glycol mixture circulated daily from 08:00 to 18:00; this constituted an active cooling system that was operational only during 2024. The elevated configuration of Group C allowed for comparison with a passive cooling system via natural airflow. The data of the solar panels output was automatically collected with an hourly resolution through Solaredge software.

Figure 3: Physical layout of groups A. B and C.

2.1.1 Group B: Active Cooling

This layout incorporates two independent pipe arrangements: one designed to cool the solar panels and a second dedicated to lowering the temperature of the coolant. These configurations are illustrated in Figures 4 and 5, respectively. The pipes are made out of a polyethylene material and are one inch in diameter.

Figure 4: Inner pipe arrangement of the active cooling system of Group B.

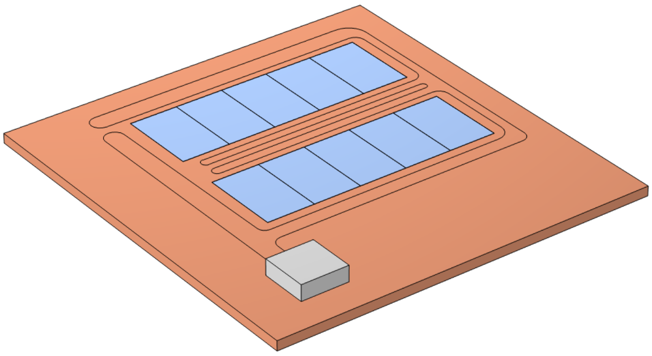

Figure 5: External arrangement of pipe system which dissipates the heat collected by the coolant running during the night.

The cooling system for the panels consists of a single polymer pipe arranged in an S-shaped path with six passes, as illustrated in Figure 4. Each pass runs horizontally across a row of five panels, turning 180° at each end to create a continuous serpentine loop. The pipe is laid over a sand bed without being fixed to the ground or the panels. The coolant circulates continuously through this pipe from 08:00 to 18:00, absorbing heat from the panels through a convective heat transfer. While the coolant keeps running, it drives the excess of heat out of the system reducing their temperature. After 18:00, the flow is redirected onto the second pipe system, which cools the fluid using ambient night air until circulation resumes the next morning at 08:00.

The coolant mixture (water-glycol) was selected for its handling safety, low environmental impact in the event of a leak, and other favorable thermal properties. Glycol specifically has a boiling point of 198 °C and a freezing point of −37 °C[17]. This represents an advantage in extreme environments, such as deserts, where day-time temperatures can be extremely high while night-time temperatures may drop below freezing, preventing the running liquid from both evaporating and freezing.

The external pipe system, used to cool the fluid during the night-time hours (18:00–06:00), lays exposed to the ambiance on a stack of metal sheets and insulating foam. The layer configuration (foam, metal, and pipe) is illustrated in Figure 3. As represented in Figure 5, the coolant enters the external piping system from a reservoir (represented as a gray box in the figure), it circulates around and between the PV matrices, and finally exits the system back onto the reservoir it was pumped from. In this implementation, the piping lay above surface, which is considered as sufficient for cooling off the coolant due to the small scale of the experiment and the geographical location of the setup (southwest Finland). For more advanced setups, the piping is meant to be placed underground for more efficient cooling of the liquid.

2.2 Model

2.2.1 Overview

The following section provides a detailed description of the computational model developed to simulate the Finnfoam layout under Finnish environmental conditions. This will establish the baseline for all subsequent model variations, which involve adaptations for different geographical contexts or other optimized configurations.

Initially, a general overview of the model is presented, where various specifics and other justifications are omitted on purpose; these are elaborated in the subsequent *reasoning* section. The derivations of the model will be explicitly detailed in a different section. Any modeling aspect not specifically mentioned for the variation can be assumed to be identical to that of the Finnish base model.

A computational model was developed as illustrated in Figure 6 to replicate the physical pipe configuration of the active cooling system used in Group B. This model is designed not only to simulate the coolant flow dynamics but also to incorporate and analyze the effects of varying environmental parameters, such as solar irradiation and ambient temperature. However, this model does not account the external arrangement of pipes which lower the coolant temperature overnight.

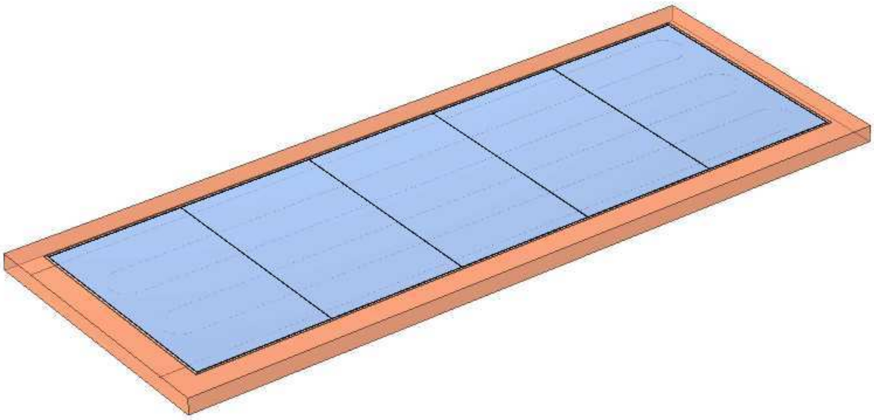

Figure 6: Model of group B constructed with COMSOL Multiphysics.

The accuracy of the model is first validated by comparing its results with empirical operational temperature data for PV panels in Accra, Ghana, as reported by Khalis M. et al. [18]. Their study provides average ambient and panel operating temperatures over a two-year period for several types of solar panels. Following the successful validation, the model is applied to simulate conditions in southwestern Finland and subsequently for a case study in Spain. In Figure 7, the locations used for both, validation and cases of study are presented for reference. The objective of determining optimal parameters for both, coolant and geometry, such as initial velocity and inlet temperature, as well as the number of passes required to maintain the photovoltaic panels at a near operational temperature of 25°C.

(a) (b)

Figure 7: Locations used for the (a) validation of the model and (b) cases of study. Map sourced and adapted from Wikimedia Commons [19].

The model geometry comprises three primary substructures that can be identified in Figure 6: ground domain (orange surface), panel arrangement (blue sections), and piping system (black line under the panels). The piping system is positioned between the ground and the solar panel arrangement, ensuring direct thermal contact with both. For simplicity, a dedicated structure acting as an aluminium frame or insulating foam was left out, and the sides of the panel were set as perfectly insulating.

The panel array comprises five solar panels, each with dimensions of 0.992 m x 1.636 m x 0.04 m. Each panel is modeled as a geometric stack of five distinct layers with separate material properties (Glass, encapsulant, solar cells, encapsulant, and backsheet).

The piping system is embedded within the ground, such that the top of the pipe is in perfect thermal contact with the bottom of the panels, with no air gaps at any material interfaces. By default, the material is set as a polymer (PVC) to resemble the original conditions.

As illustrated in Figure 8, the piping system features a single coolant entry and exit point. The pipes are arranged horizontally in straight, parallel segments, connected by U-bends to form a serpentine path consisting of six consecutive lengths before the outlet.

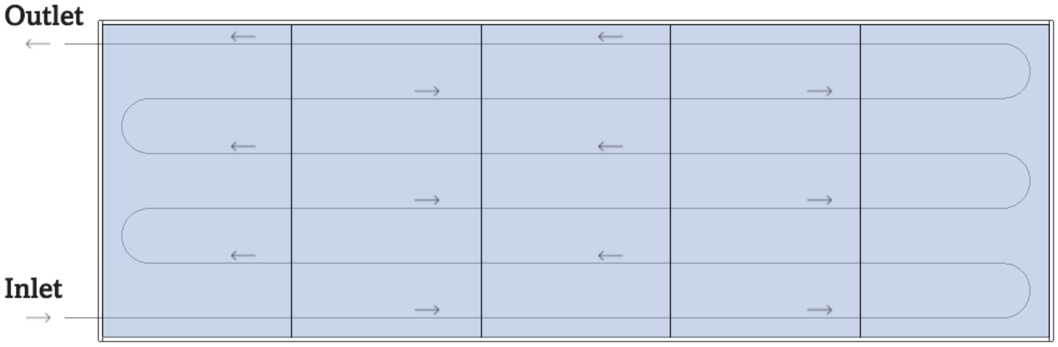

Figure 8: Pipe system under the solar panels.

The pipe material was initially set to polymeric values to reflect the conditions of the physical experiment. When exploring potential system optimizations, copper was introduced to evaluate its thermal performance within the same configuration. Both materials were adapted using the COMSOL material library, with additional properties such as thermal conductivity (κ) and surface roughness (R)—absent from the default database —manually specified. These details are summarized in Table 1.

Table 1: Properties of Copper and PVC.

Material	κ **(**W/(m · K)**)**[20]	R**(mm)**[21]
Copper	413	$0.001 - 0.002$
PVC	0.19	$0.0015 - 0.007$

The project is modeled as a time-dependent study from 06:00 to 20:00 hours, in which ambient temperature and solar irradiance of an average summer day are implemented as interpolated functions, with data sourced from the EU Photovoltaic Geographical Information System (PVGIS) [22]. The above-ground surfaces are exposed to both: solar radiation and the ambient air (modeled as natural convection, i.e. as perfectly still air).

The solar radiation source in the COMSOL model is defined for each specific study location using its geographical coordinates (latitude and longitude). These coordinates enable COMSOL to accurately calculate the sun's position (azimuth and elevation angles) over daytime. For instance, a case study placed in Helsinki utilizes solar irradiance data and solar path calculations corresponding to June 2022, along with its specific geographical coordinates: latitude 60.192059 °N, longitude 24.945831 °E. All simulations are performed assuming optimal, clear-sky conditions. Effects such as shading from surrounding objects and the explicit separation of solar radiation into direct and diffuse components are not considered in the current model.

The simulation results illustrate the thermal behavior of various modeled components, including the panel bodies, the piping system, the coolant upon completing its circulation path, and the ground surface. The resolution can be set for minutes to hours for a single day.

2.2.2 Reasoning

Simplification of the Geometry

Although the physical setups for Groups A and B included lateral insulating foam, its effect was found to be negligible in the simulation. The inclusion of a dedicated insulation structure around the panel produced a minimal cooling effect, reducing the temperature by only 0.035 °C. Consequently, the side surfaces of the panels were treated as perfectly insulated in the computational model, focusing the thermal analysis on the top and bottom surfaces.

Additionally, the initial models included a deliberately thick aluminum frame to evaluate its potential impact on heat capacity by the frame material. These analyses demonstrated that such contributions were insignificant (with a similar 0.055 °C change in temperature) to the overall thermal performance of the model. This finding is attributed to the typically slender profile of actual panel frames relative to the total panel surface area and thermal mass. Therefore, the frame was omitted from the final computational model to maintain geometric simplicity, confident that this would not affect the accuracy of the primary heat transfer analysis.

To ensure that the thermal effect of the ground was correctly modeled, its domain size was also investigated. An initial simulation with a small ground domain of 1 m lateral offset (exposed earth area around the panel) and 0.2 m depth, revealed that the direct solar heating caused a significant temperature increase of the domain. Due to the domain's relatively low thermal mass, this led to the hypothesis that the unrealistically warm ground could be reducing the coolant system's effectiveness by acting as a secondary heat source.

To investigate this, two additional simulations were performed: one with a larger domain (20 m offset, 60 m depth) to represent real-world conditions, and another with a zero-offset domain to eliminate direct solar heating of the ground. Unexpectedly, all three cases produced similar results within a margin of ±0.2 °C, demonstrating that the size of the earth domain, within realistic bounds, did not significantly affect the outcome. It should be noted, however, that the earth domain itself was a necessary modeling requirement, as the piping system must be embedded within a surrounding domain.

Solar Panel Structure

The panel layer properties are based on a Leow, W. Z. research [23]. The material properties for these layers include thickness, thermal conductivity (κ), specific heat capacity (c), and density (ρ), detailed later in this chapter in Table 2.

The solar panel is modeled as a composite structure comprising five distinct layers, arranged in ascending order from the $z = 0$ reference plane: Tedlar (backsheet), an initial Ethylene Vinyl Acetate (EVA) layer, a crystalline silicon layer, a second EVA layer, and tempered glass (top cover). The specific thicknesses and thermal properties for these five panel layers were manually defined based on data sourced from the previously mentioned W. Z. Leow et al. [23] study.

Table 2: Materials and properties of each layer.

Layer	**Material**	**Thickness** (cm)	$\boldsymbol{\kappa}$ (W/mC)	**c** (J/kgC)	$\boldsymbol{\rho}$ (kg/m^3)
Glass Covering	Glass	0.3	1.8	500	3000
Encapsulant (EVA)	Elvax 260	0.05	0.35	2090	960
PV Cell	Silicon	0.04	148	677	2330
Encapsulant (EVA)	Elvax 260	0.05	0.35	2090	960
Backsheet	Tedlar	0.01	0.2	1250	1200
Aluminum Frame	Aluminum	2.0	204	996	2707

Materials

The material properties for the model components are primarily sourced from the COMSOL materials database. For example, 'Generic soil' with its predefined thermal characteristics is used for the ground domain, and properties for 'Generic plastic' tubing are used for the pipes. However, the coolant, is set at 40% ethylene glycol-water mixture; its thermophysical properties were obtained from an external source [24] and listed in Table 3. The detailed material specifications for the panel's layered composition are presented in Table 2.

Table 3: Coolant parameters of a water-glycol mixture at 40% concentration.

Parameter	**Value**	**Unit**	**Description**
C_c	3.626	$kJ/(kg * K)$	Heat capacity
μ_c	2.2	$mPa * s$	Dynamic viscosity
ρ_c	1063	kg/m^3	Density
c_{pc}	3.647	$kJ/(kg * K)$	Specific heat
κ_c	0.258	$W/(m * K)$	Coolant thermal conductivity

Initial Temperature

The initial temperature of the entire system is set to ambient temperature. This stems from the observation that the PV panels respond rapidly to the changes in solar irradiance and ambient temperature. Mainly due to their relatively low thermal capacitance. This rapid response means that the panel temperatures are predominantly dictated by current environmental conditions and the active cooling effect.

Coolant

The state of the coolant begins at atmospheric pressure with no tangential velocity. Its circulation within the piping system follows a daily schedule: it is active between 08:00 and 18:00 hours, and inactive (coolant velocity of 0 m/s) at all other times. This operational window is strategically extended to study the impact of active cooling. During the operational period, the coolant is introduced at an inlet velocity of 1 m/s and an inlet temperature of 10 °C.

The fluid dynamics and thermal behavior within the piping system are modeled using COMSOL's Non-Isothermal Pipe Flow interface, which computes the coolant's temperature change as it passes through the system. The pipe walls are defined with a thickness of 2 mm. This model incorporates two key characteristics of the pipe wall material: its surface roughness and thermal conductivity, with values derived from the specified material.

Radiation Implementation

Solar radiation effect is modeled using the surface-to-surface radiation interface of COMSOL, which models heat transfer between surfaces. Most of the solar radiation that reaches earth varies within a spectrum from infrared to ultraviolet ($300 - 2500\ nm$)[25] and naturally, each material layer in a solar panel reacts differently to these wavelengths (e.g., absorption, transmission, and emission) across this spectrum [26]. Therefore, a detailed layer-by-layer optical model, including internal scattering and absorption, would require excessive computational resources. The primary objective of this study is to accurately capture the overall thermal behavior of the panel due to solar radiation, rather than to resolve the precise internal energy distribution pathways within the multiple layers. To solve this, a simplified model is presented.

This approach replaces the detailed simulation of how solar radiation interacts with each individual layer of the panel by instead assigning effective, wavelength-dependent solar absorptivity values exclusively to the top layer (tempered glass). For this simplified surface radiation model, the panel layers are then purely treated as opaque from the perspective of the external radiation interface. The goal of this simplification is to achieve a similar heating effect of the panel as compared to physical reality in a way that circumvents the challenge of accurately modelling the intricate ray tracing and energy deposition within the various semi-transparent layers.

Crucially, these effective spectral absorptivity values for the top surface were not arbitrary. They were determined through an iterative calibration process, validated against published experimental data on PV panel operational temperatures (discussed later) to ensure that the modeled thermal response accurately reflects empirical observations.

The derived effective spectral absorptivities (α_λ) assigned to the panel's top surface for different solar wavelength bands are presented in Table 4.

Table 4: Effective spectral solar absorptivities for the PV panel top surface.

Wavelength Range (µm)	**Effective Absorptivity (α_λ)**
$0 - 1.1$	0.93
$1.1 - 2.5$	0.40
> 2.5 (up to ∞)	0.80

This spectral division and the assigned absorptivity values are informed by the typical solar energy distribution and the radiative properties of PV solar cells materials [27]. The majority of useful solar energy conversion in photovoltaic cells occurs from radiation in the $0 - 1.1$ μm range; beyond approximately 1.1 μm, the direct absorption in silicon cells drops significantly, since silicon is an indirect band gap semiconductor[28].

The $1.1 - 2.5$ μm spectral band, however, still contains a notable portion of solar energy (approximately 20%), this is accounted by the effective absorptivity of the top surface in the model[27]. Beyond 2.5 μm, common PV materials like silica glass and Tedlar backing become largely opaque [29], which is reflected in the higher effective absorptivity for that spectral region. This heuristic approach ensures that the total solar energy absorbed and converted to heat by the panel is represented as accurately as possible relative to real-life conditions.

Initially, the simulation assumed a blackbody environment, which resulted in a significant overestimation of the heating effect on the panel. Consequently, a more refined approach was adopted by calculating the emissivity of the environment separately. Assuming the ideal, clear-sky conditions of the simulation, the emissivity was derived using the Clark and Allen formula [30]:

$$\epsilon_{sky\ clear} = 0.787 + 0.764\ \ln\left(\frac{T_{dp}}{273}\right) \tag{1}$$

where T_{dp} is the dewpoint temperature in Kelvin, i.e., the temperature in which the air must be cooled for its water vapor to turn into liquid dew or fog.

For a moderately humid day, represented by a dewpoint temperature of 5 °C, the formula is evaluated as follows:

$$\epsilon_{sky\ clear} = 0.787 + 0.764\ \ln\left(\frac{5 + 273.15}{273}\right) \approx 0.8 \tag{2}$$

2.2.3 Validation of the model

The model's solar absorption heuristic was next compared against experimental data to validate and adjust the effective absorptivity (α_λ). This validation was performed using values from a study by Khalis et al.[31], which reported the peak operating temperatures of four types of PV panels -one monocrystalline, two polycrystalline, and one amorphous- over a two-year period across three different seasons in Accra, Ghana.

In the study by Khalis et al.[31], panel temperatures were automatically recorded every five minutes and categorized into three key seasons relevant to the local climate. The average peak temperatures and the corresponding times of day were then reported and are presented in this thesis in the first four rows of Table 5. Additionally, dispersion plots of the average temperatures for each panel type were included in their report, which served as a reference to calibrate the thermal response of the simulated panels to ambient conditions in this study.

For the purpose of model calibration, data selection was guided by the project's objective to assess cost-effective solar solutions and by the crystalline silicon structure of the panels modeled in this work. Consequently, only data relating to polycrystalline panels from the aforementioned study were utilized. Data from monocrystalline panels were excluded due to their generally higher cost, while amorphous panels were not considered due to significant differences in their material composition and thermal behavior. Additionally, measurements taken during rainy seasons were omitted from the calibration dataset, as the current simulation model does not account for precipitation and significant changes in diffuse radiation associated with heavily clouded conditions.

The calibration process itself began by focusing on a specific dataset: the *Polycrystalline I* panel performance during the Harmattan season reported by Khalis et al.[31]. The report included specifications on operational conditions of this case-season, hours of operation, ambient temperature, and geographical location-, corresponding ambient temperature and solar irradiation profiles were compared and retrieved from PVGIS; these detailed data profiles are presented in Appendix A.

Harmattan season is comprise of the months of December and January, after careful comparison, January data from PVGIS [22]-general horizontal solar irradiation (GHI) and ambient temperature- were selected for this specific calibration, as they most closely aligned with the documented ambient temperatures and relevant hours of the 'Polycrystalline I' Harmattan season case. These January profiles were subsequently used as inputs for the computational model. The parameters of the panel's solar absorption heuristic (Table4) were then iteratively adjusted until the simulated peak panel temperature closely matched the peak temperature and hours reported in the empirical study for this specific scenario.

Following this adjustment, a satisfactory resemblance between the model's predicted temperatures and the reported empirical data was achieved for this initial calibration case, as illustrated in Figure 9. The set of effective 'emissivity' parameters derived from this process was then fixed at as shown in Table 4 for subsequent validation steps.

To further evaluate the robustness of the calibrated absorption, these fixed 'emissivity' parameters were then applied to simulate other distinct cases from the Khalis et al.[31] study, using their respective PVGIS-derived temperature and irradiance profiles. These additional validation cases included the 'Polycrystalline Panel I' during the dry season, and the second polycrystalline panel type (referred to as 'Polycrystalline Panel II') during both, the Harmattan and dry seasons. The comparison of simulated and reported peak temperatures for these further validation cases is summarized in Table 5b.

Table 5: Comparison of reported and simulated values for solar panels.

(a) Values for polycrystalline panel I [31] and simulation.

		Poly I		**Simulation**	
Time	**Season**	**Peak Temp °C**	**Ambient Temp °C**	**Peak Temp °C**	**Ambient Temp °C**
12:30	Harmattan	65.4	33	65.8	32.7
12:30	Dr	54.25	31.71	60.86	31.77

(b) Values for polycrystalline panel II [31] and simulation.

		Poly II		**Simulation**	
Time	**Season**	**Peak Temp °C**	**Ambient Temp °C**	**Peak Temp °C**	**Ambient Temp °C**
11:30	Harmattan	65.1	34.3	63.74	33.6
13:00	Dry	54.7	31.94	55.1	32.4

As observed from the validation tables, the peak temperatures reported in the simulation differ from the empirical data by approximately $\pm\mathbf{3.1}\,^{\circ}$C. This margin of error should be considered when using the simulation to make assessments regarding optimal operating temperatures, particularly when evaluating the addition of a cooling system. Several effective 'emissivity' values close to the final adopted value were tested; however, the current set of parameters was ultimately selected because it consistently produced the smallest and most balanced deviations (i.e., both positive and negative) from the reported empirical data.

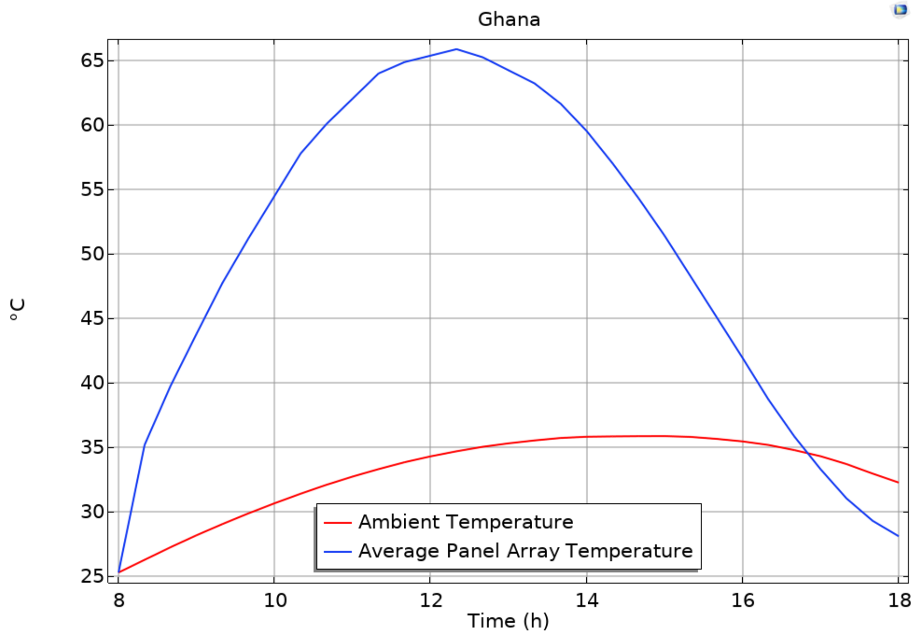

Figure 9: Thermal behavior of a polycrystalline solar panel in Ghana, Accra.

2.3 Study cases for the computational model

Three different case studies were conducted using the model: one with the specifications of Group B, one in Helsinki, and another in the Tabernas Desert. For the Group B and Helsinki cases, consistent input profiles were used for the sun's path, solar irradiation patterns, and ambient temperatures. while for the case of the Tabernas Desert, these parameters were adjusted to reflect the different environmental conditions of that location.

In the Group B case, the focus is on how the active cooling system affects the panel's thermal behavior throughout an average sunny day during the hottest month. This includes comparing panel temperatures with and without cooling, and analyzing the coolant's outlet temperature.

The Helsinki and Tabernas Desert studies, in contrast, evaluate the same initial system parameters for both cases -initial velocity and coolant pressure, and pipe configuration- with the difference of climatic conditions and irradiation of each location. These simulations also explore how to optimize the cooling system for each environment, with the aim of maintaining panel temperature near the ideal operating point of 25°C. Optimization parameters include adjustments to coolant inlet temperature, pressure, and velocity, as well as changes to pipe geometry and material.

The Tabernas Desert case was carefully selected to meet the project's goal of evaluating the cooling system's performance in a hotter climate, since the presence of high temperatures and solar exposure of this location provides a meaningful contrast with the base model.

According to Access to Solar Radiation Data for Spain (ADRASE by its Spanish acronym)[32], the regions presenting the highest annual averages of daily values of GHI comprise the southern region of the Iberian Peninsula, excluding the Balearic and Canary Islands. Specifically, in the surrounding region of Almeria, where the Tabernas Desert is located, the global average reaches up to 8 ($kWh/m2$), outstanding from other regions of mainland Spain.

To support more broadly the importance of accounting the local conditions for this study, it is illustrated in Figure 10 the monthly GHI and the average ambient temperature recorded in 2023 across three locations -Helsinki, Tabernas Desert, and a Northern Sahara point near El Oued, Algeria-. This last location is merely used to contrast the differences of irradiation and temperatures among different geographical coordinates. Additionally, Figure 11 shows a geographical reference map with typical GHI distribution patterns. Both the data used for plotting and the map were sourced from PVGIS [22].

Figure 10 shows a general trend: as monthly solar irradiation increases, particularly in summer, the average ambient temperature also tends to rise. The data indicate significant differences in annual solar irradiation between these locations.

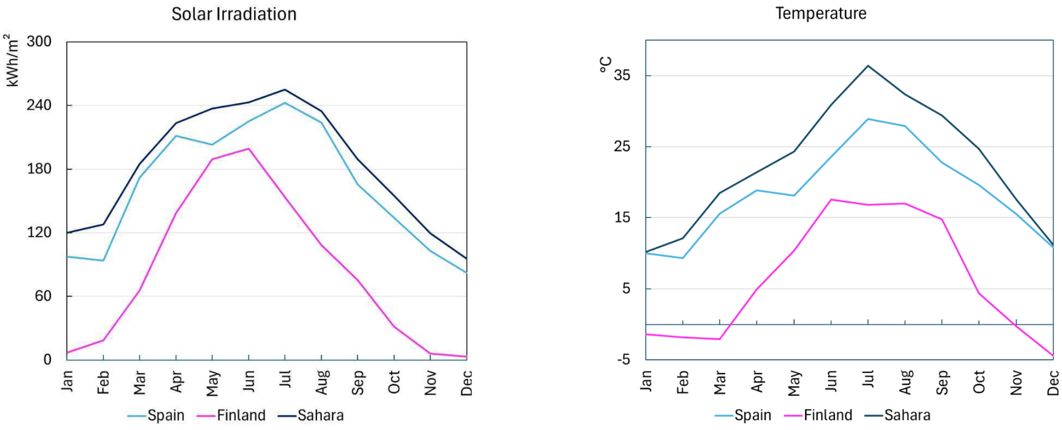

(a) (b)

Figure 10: (a) Total monthly irradiation, and (b) Average monthly temperature.

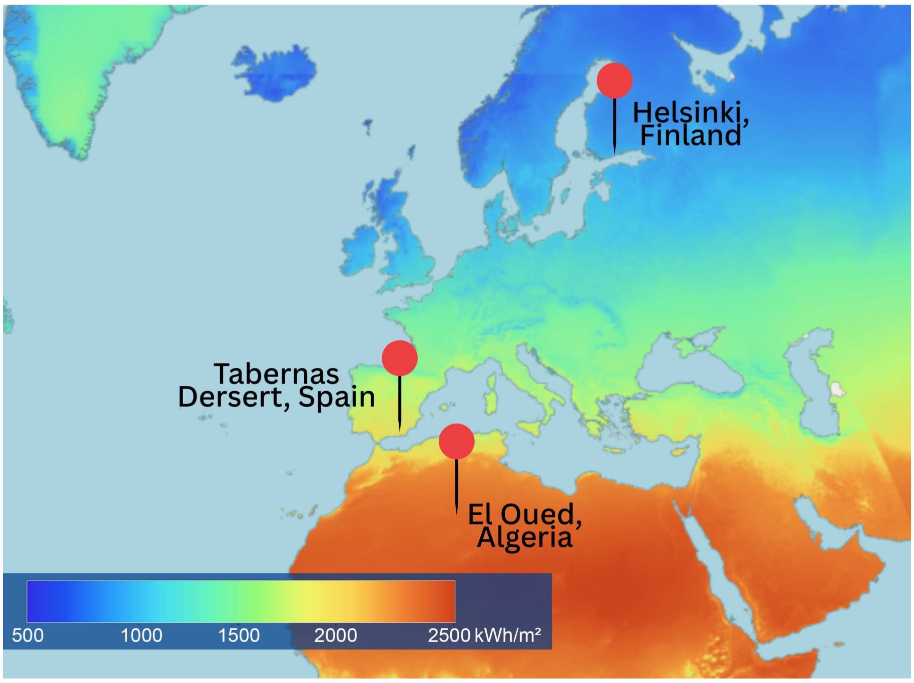

Figure 11: GHI distribution and reference points. Map retrieved and adapted from PVGIS [22] [33].

For example, the northern Sahara location received nearly 2200 kWh/m^2 annually, and the Tabernas Desert (Spain) received about 2000 kWh/m^2. In contrast, Southwest Finland received only around 1000 kWh/m^2. This means Southwest Finland received about 51% of the irradiation of the Tabernas Desert and roughly 45.6% of that recorded for the northern Sahara.

These examples highlight that higher solar irradiation generally leads to significantly higher average ambient temperatures. However, it is important to understand a limitation of the temperature data in Figure 10(b): it displays only monthly averages. Therefore, actual daily maximum temperatures, which can be much higher and are critical for assessing panel overheating, are not shown in this particular figure.

Based on the information in Figure 10, specific periods were chosen for detailed case studies: June for Group B and Southwest Finland (Helsinki), and July for Spain (Tabernas Desert). These months had the highest average solar irradiation and ambient temperatures for their respective locations. The original data profiles were generated with PVGIS [22] and can be found in Appendix B.

3 Results

3.1 Physical layout

The monthly performance of the entire system is presented in Figure 12. The three groups (A, B and C) began operation in the last week of June 2022. By this time, the active cooling system was not yet implemented for group B, but until late May of 2024. The figure also shows a data gap between October 2023 and March 2024, due to a temporary stop of operations; plant operations resumed in April 2024. Following the resumption of operations (i.e., after April 2024), the cooling system was installed under the panels of group B and remained active until November 2024. As a result of the disruption in measurements, only data from the July-September period of each year will be considered as relevant months for this study.

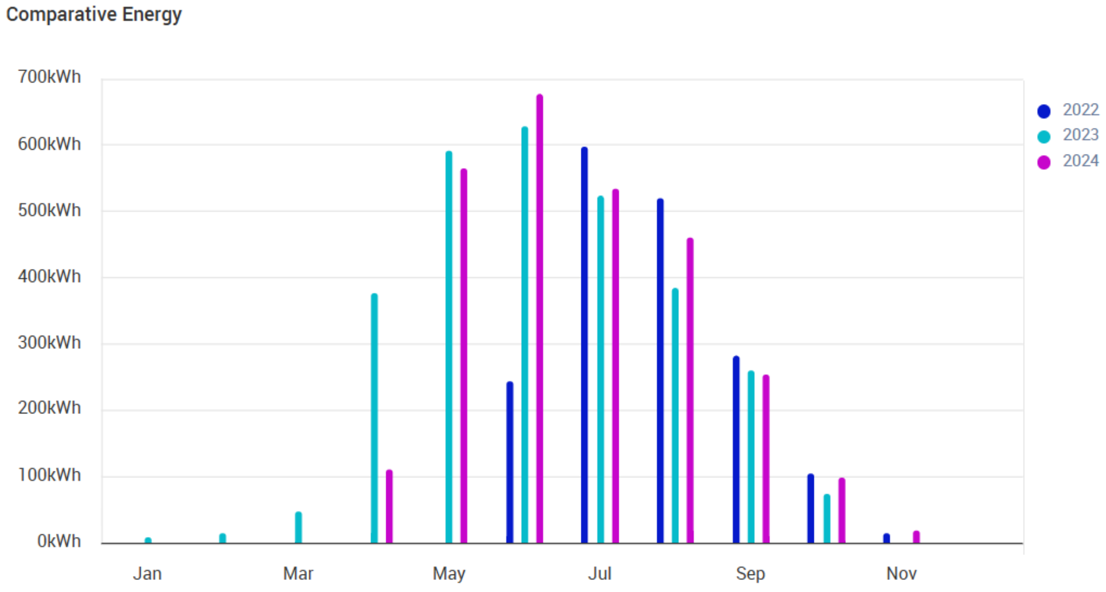

Figure 12: Monthly average power output of the three groups for years 2022-2024.

According to the values reported in Figure 12, the total energy produced during the months of interest in 2024 -July to September- increased compared to that in 2023, but it did not surpass the production levels of 2022. Another important observation is that the registered maximum output tends to decrease from year to year; for August 2023, in particular, a more significant drop in output is observed. For this latter case (August 2023), the data were manually reviewed, and there were no signs of an interruption in panel operation. Therefore, these two phenomena could be explained as follows:

1. The efficiency of solar panels is estimated to have a yearly degradation rate of 0.6-0.7% [34].
2. The amount of solar radiation received by the panels can vary from year to year, even when measured during the same season, due to climatic variations such as differences in the number of rainy or cloudy days.

To support the second point, Figure 13 presents the average monthly temperature and GHI for Salo, Finland, during the years 2022 and 2023. A noticeable drop in both temperature and irradiance can be observed for August 2023 compared to the same month in 2022. Data for 2024 is not included, as the source used for this analysis—PVGIS [22]—has not yet been updated with the most recent values.

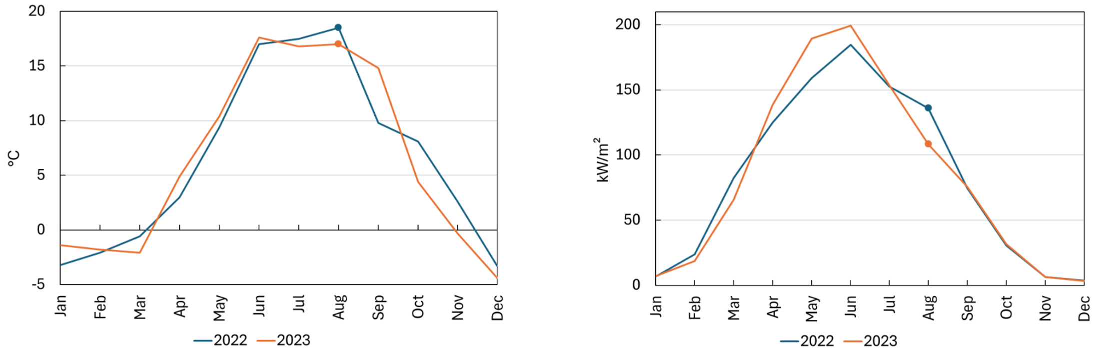

(a) (b)

Figure 13: Average Monthly Ambient Temperature and Irradiation Profiles (2022-2023) in Salo, Finland. (a) Ambient Temperature; (b) Irradiation

3.2 Comparison between Groups A, B and C

3.2.1 Temporal Analysis

Although Figure 12 illustrates the overall energy behavior of the three combined groups, a more detailed analysis is provided in Figure 14. This figure shows the individual power output (kW) from July to September for the years 2022 to 2024, highlighting the performance differences among the groups with distinct cooling strategies. To recap: Group A was installed at ground level without any cooling; Group B, also at ground level, used active cooling; and Group C was elevated on structures to enable passive cooling via natural air flow beneath the panels.

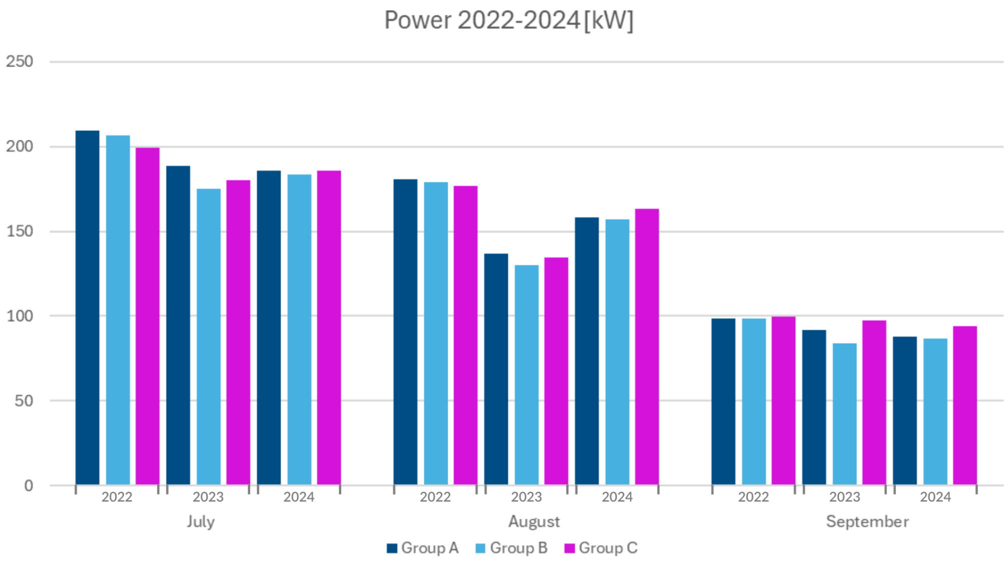

Figure 14: Monthly power yield per group for the years 2022–2024.

Group C was the only panel array equipped with a cooling system throughout the entire experimental period. Consequently, it was anticipated that Group C would consistently outperform groups A and B, particularly during the initial two years when these operated without any cooling assistance. However, this expectation was not consistently met by the performance data. As shown in Figure 14, Groups A and B registered higher power outputs than Group C during July and September of the first year of operation. In fact, group C only outperformed Group A in approximately 50% of the recorded instances.

To more accurately compare the performance of the different groups, particularly Group B in 2024 (following the installation of its cooling system), a data normalization process was undertaken. This involved scaling the 2024 output data for Group B against the average output for the previous years (2022 and 2023). Such normalization allows for an evaluation of relative performance improvement, rather than relying solely on absolute output values. The normalized output is calculated using the following expression:

$$Normalized\ Output(\%) = \frac{Average\ 2023\ Output}{2024\ Output} 100\%$$

The results, summarized in Table 6, indicate a clear performance improvement for every group when comparing 2024 with 2023, though not when comparing 2024 with 2022. Furthermore, Groups A and C individually showed higher output gains compared to Group B. Since Groups A and C had no operational changes in 2024, this observation could suggest that weather conditions in 2024 may have contributed significantly to increased energy yields across all groups.

Table 6: Ratio comparison of total power performance of each group for the years 2022-2024.

Year	**Group A**	**Group B**	**Group C**
2024/2022	89.43	88.61	91.76
2024/2023	106.25	105.28	109.03

Moreover, the difference in performance of Group B compared to the other groups is shown in the first two rows of Table 7. The consistently lower power output from this group may be attributed to limitations in the system design. Specifically, if the pipes of the cooling mechanism do not make direct contact with the surface of the panels, this may limit the system's effectiveness in reducing operating temperatures and, consequently, in improving power output.

Table 7: Yearly power difference between groups for the years 2022-2024

Group	**2022**	**2023**	**2024**
B/A	0.99	0.94	0.99
B/C	1.01	0.97	0.97
C/A	0.98	0.97	1.02

3.3 Study cases of the computational model

The simulation of Group *B* was run with the initial parameters discussed in the previous section and summarized in Table 8. The base configuration of the pipes consisted of six fixed passes. Next, an optimization study was performed for the Helsinki and Tabernas Desert case studies. This involved investigating how the panel temperature responds to variations in initial coolant parameters (pressure, velocity, and temperature) as well as to changes in the number of passes within the pipe arrangement. However, variations in the initial velocity and pressure of the coolant did not yield a significant impact on panel temperature reduction. Changing the pressure and velocity from 1 to 3 Pa and m/s, respectively, resulted in only a 0.03 °C temperature difference in both cases. Therefore, to avoid unnecessary energy consumption—since higher pumping effort would reduce the panel's net energy output—the values were kept at 1 Pa and 1 m/s.

Table 8: Variable parameters used for the model case studies.

Parameter	**Value**	**Unit**	**Description**
T_{0c}	$0-5-10$	$°C$	Coolant initial temperature
ν_{0c}	$1-3$	m/s	Coolant initial velocity
P_c	$1-3$	Pa	Coolant pressure

Therefore, only the results pertaining to the number of pipe passes and the initial coolant temperature are reported in detail here. Other simulation parameters remained as described in as the same for Group *B* (Table 8). For each case study, the corresponding location-specific ambient temperature, solar irradiation profiles, and geographical coordinates were applied and can be revised in the Appendix B.

Figure 16 presents a COMSOL-generated illustration of the thermal behavior of the panel string at 14:00, with the active cooling system in operation. The image shows a transverse cross-section where the bottom of the panels meets the piping. A logarithmic temperature scale is used to emphasize the temperature differences between the panels and the cooling pipes. After six hours of continuous coolant flow, the panels still present an uneven temperature distribution, with noticeably lower temperatures along the pipe paths.

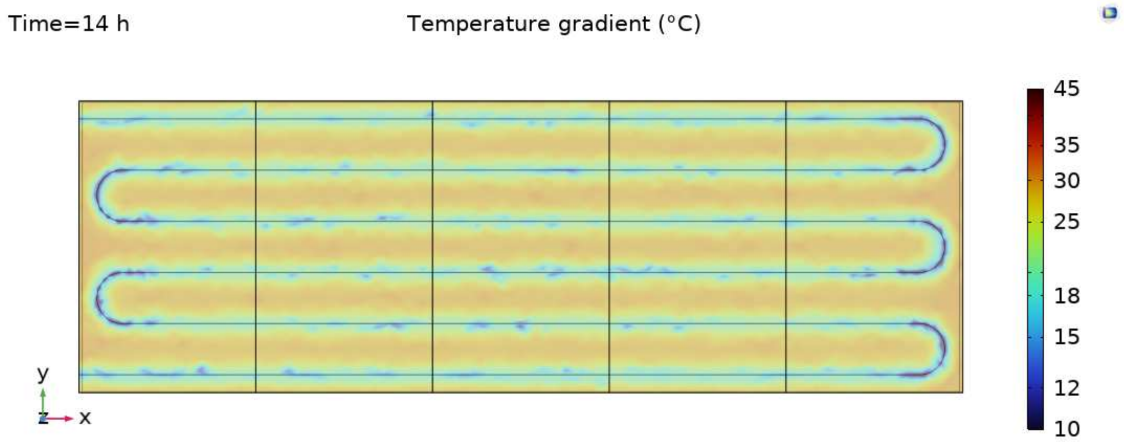

Figure 15: Thermal behavior of Group *B* at 14:00.

3.3.1 Group B

The results of the simulation for Group *B* are presented in Figure 16, where the operational temperature of the solar panel is illustrated for conditions when the cooling system is both active and inactive, along with the ambient temperature provided as a reference. The active case is divided in two sub-cases; plastic pipes and copper.

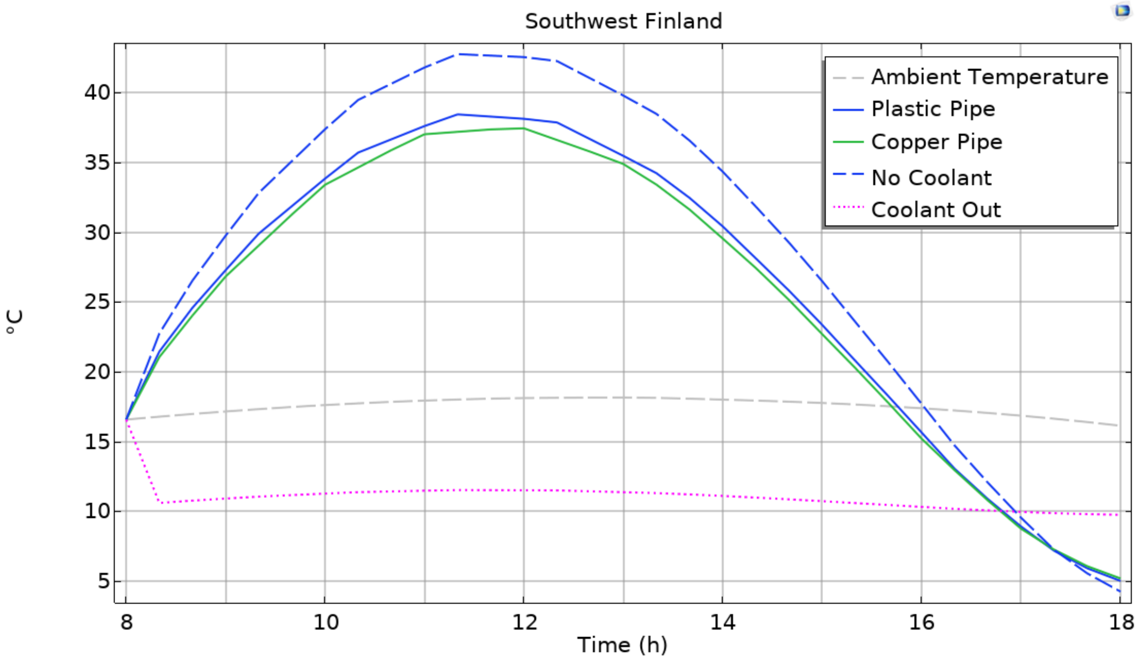

Figure 16: Average temperature curves of ambient and panel set with and without coolant for a June day in southwest Finland.

In the scenario with active cooling, coolant circulation begins at 08:00 hours with an inlet temperature of 10 °C. Under these conditions, the simulation shows that activating the cooling system reduces the peak panel operating temperature from 42.8 °C (observed without cooling) to:

- 38.45 °C with a plastic pipe.
- 37.45 °C with a copper pipe.

A decrease of approximately 4.35 °C in the peak operating temperature is observed when the plastic cooling system is active, demonstrating that, under these ideal simulated conditions, the system effectively reduces the panel's operating temperature. The copper piping only improved the reduction of temperature by 1 °C.

The coolant output temperature, represented by the magenta dotted line, exhibits an abrupt change between 8:00 and 9:00. This is a simulation artifact which can be explained as follows. The simulation begins with the pipe system already filled with stationary coolant at ambient temperature. When the flow starts, new coolant entering at 1 m/s reaches the outlet very quickly relative to the total 10-hour simulation window. Ideally, this rapid temperature change would appear as a near-vertical line on the graph. However, the plot shows an artificially steep slope because the solver's large time step (10 minutes) visually "stretches" the near-instantaneous event over the duration of a full step, exaggerating its time scale.

3.3.2 Helsinki and Tabernas Desert

Due to minimal performance gains observed when varying coolant velocity and pressure, all simulations presented here used standardized values of 1 m/s and 1 Pa to maintain consistency and simplicity. The model was executed a total of 16 times per location, covering three different coolant inlet temperatures and five variations in the number of pipe passes. Figure 17 presents the peak panel temperatures for each variation, plotted against the number of pipe passes. The curves presented revealed a non-linear behavior as the number of passes increased.

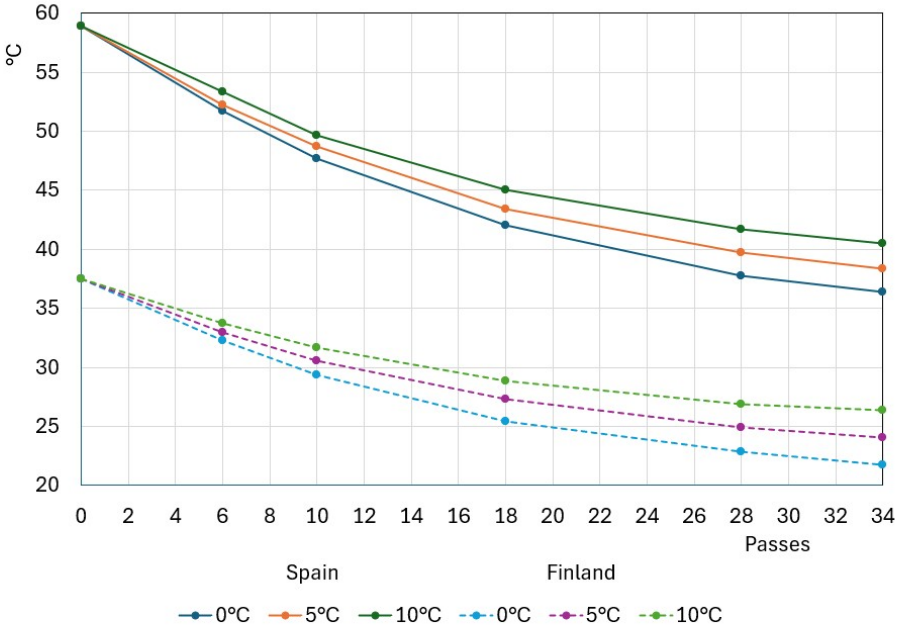

Figure 17: Peak operating temperatures in function of coolant temperature and number of swipes in the piping system. The straight lines correspond to Tabernas Desert, and the dotted lines to Helsinki.

In Helsinki, the highest panel temperature (no cooling) was 37.24 °C, while the lowest achieved was 20.6 °C, corresponding to 37 pipe passes and a coolant temperature of 0 °C. However, the desired operating temperature of 25 °C could be reached with less intensive configurations, specifically, the cases of 22 passes at 5 °C or 16 passes at 0 °C.

In contrast, the Tabernas Desert case showed significantly higher thermal loads. Without cooling, the peak panel temperature reached 58.68 °C. Even under the most aggressive cooling configuration (36 pipe passes and coolant at 0 °C), the lowest panel temperature achieved was 34.36 °C, still well above the optimal 25 °C threshold.

3.4 Comparison between computational model and real set-up

The real experiment used a pipe layout with 6 passes. When this configuration was replicated in the model, it resulted in a peak temperature reduction of only 4.25 °C. This modest improvement is considered not particularly cost-effective in locations with similar conditions to the southwest of Finland, especially when factoring in the continuous energy demand required to maintain active cooling—both during the day to cool the panels and at night to chill the coolant.

In some simulation cases, over 34 straight pipes were implemented to explore how increasing the pipe coverage area influences the thermal behavior of the solar panels. While useful for understanding the system's limits, in real life it leads to diminishing returns and introduces practical challenges due to increased material costs and limited available space.

The contrast in the cases of Finland and Spain demonstrated that the cooling system shows a greater relative performance in hotter environments when operated under similar conditions. Specifically, when comparing the two locations under their most effective cooling scenarios (i.e., 34 passes and 0°C for the coolant), the peak temperature reductions of 16.55°C and 24.31°C were achieved in Helsinki and Spain, respectively.

In Helsinki, it was feasible to maintain panel temperatures below 25°C using for the following configurations:

- Coolant at 10°C with 34 pipes.
- Coolant at 5°C with 18 pipes.
- Coolant at 0°C with 6 pipes (baseline configuration).

However, when the same conditions were applied to the Tabernas Desert case, the temperature reduction was over 10 °C less effective compared to the Helsinki case. Nonetheless, the overall thermal reduction in Spain was still greater, as the temperature difference between the coolant-on and coolant-off scenarios was approximately 6 °C larger than in Helsinki, underlining the improved cooling efficiency in hotter climates.

Notably, the use of monocrystalline panels in hot climates may yield better performance than polycrystalline panels, as suggested in the literature [31].

3.5 Optimization

Based on the results from the previous section, effective strategies to reduce the peak temperature of the solar panel array involve increasing the contact area between the top part of the cooling pipes and the solar panels surface, and diminishing the initial temperature of the running coolant. However, both approaches present significant challenges and limitations. In the following section, each strategy is detailed, and its limitations are reviewed independently. The computational model also explored alternative parameters—such as the pipe material, initial velocity, and pressure of the coolant, but yielded only marginal improvements.

In addition, the results also showed that systems operating in hotter climates, such as Spain, benefit more from cooling technologies compared to those in cooler regions like Helsinki.

3.5.1 Increasing the pipe and panel contact area

Increasing the number of pipe passes across the bottom surface enhances the contact area and consequently the potential for heat transfer. However, this method must consider four key factors: the relationship between pipe passes and temperature, area limitation, pipe material properties, and cost-effectiveness.

As illustrated in Figure 17, the reduction in panel temperature does not scale linearly with the number of pipe passes, showing a non-linear relationship. Each curve, which represent the peak temperature of the panel for a given number of swipes, can be observed to tend to a temperature limit different than the coolant. However, this limit can not be determined, as the panel area represents a constraint and a new limitation of this method. Expressly, the number of feasible passes depends on the available area of the panel.

In addition to the limitation by the panel area, in a real-life layout, the pipe routing also represents a constraint, as it highly depends on the pipe material properties. Particularly, the material used for the piping affects the bending radius and installation complexity. Flexible polymers allow tighter curves, while rigid materials like copper require wider turns, limiting the number of passes. While the test of scenarios were copper and polymer were used for the simulation, polymeric pipe show a difference of performance of 4 degrees more in the ideal cases for Helsinki and 5° when those casaes were run in Spain.

Lastly, the cost and practicality of the system must be considered. More passes mean more material and installation labor, increasing both cost and maintenance complexity. Moreover, increasing the contact area highlights the need for direct contact between surfaces to ensure efficient heat exchange. To improve this, the application of thermal paste or adhesive is recommended. However, this introduces maintenance challenges, as permanent adhesion complicates disassembly. In systems with continuous panel arrays, accessibility to maintenance of a single panel or a localized pipe section becomes difficult and may require disconnecting larger sections of the system.

3.5.2 Coolant temperature

Operating the coolant at lower temperatures—ideally near 0 °C—significantly reduces the peak panel temperatures. However, maintaining such low temperatures introduces a new challenge, particularly considering the original project design, which aims to dissipate the thermal energy accumulated by the pipes by redirecting the coolant mass into deeper ground layers. While the temperature increase in the coolant was observed to range between 2–4 °C depending on the conditions, the primary difficulty lies in identifying an appropriate depth where the ground can serve as a sufficiently cold thermal sink. Achieving the lowest possible initial coolant temperature requires further investigation regarding the soil temperature profiles within the specific geographical region where the system will be deployed.

3.5.3 Material-cost assessment

During the simulation, two different piping materials were considered: a generic polymer, representative of materials such as polyethylene (PE) or polyvinyl chloride (PVC), and copper. PE pipes are recognized for their flexibility, chemical resistance, toughness, longevity, and lightweight properties. They perform well in both low-temperature and heat transfer applications and are environmentally favorable compared to other materials. Similarly, PVC piping offers a long service life, easy handling and installation, corrosion resistance, and is considered a cost-effective alternative among different types of polyethylene tubes. It is also suitable for outdoor applications and can be manufactured with UV stabilizers to enhance durability [35]. Copper tubing, which is commonly used in air conditioning and refrigeration systems, is known for its high thermal conductivity.

Another important consideration was cost. An analysis of the average price for each tubing material was conducted, based on prices from four common commercial suppliers in Finland. The comparison revealed that copper piping is substantially more expensive, costing 6.79 times more than PVC and 4.21 times more than cross-linked polyethylene (PEX), respectively (the specifics of each supplier can be found in Appendix C). It should be noted that these figures reflect consumer-level retail pricing; costs may be lower for commercial or industrial-scale purchases. Furthermore, this analysis only includes the cost of the tubing itself and excludes accessories like fittings, which are a significant additional expense for rigid materials such as copper.

Therefore, although the literature recommends using high thermal conductive materials like copper for optimal performance [16], simulation results showed only a minor difference—about 1 °C—between polymeric and copper tubing. Given this negligible thermal gain and the higher cost of copper, the use of polymer-based piping is recommended for practical and economical implementation.

Given these considerations, a cost-effective and efficient thermal management strategy would likely involve the use of a polymeric pipe and a combination of both previous approaches, increasing the contact area between the piping and panel surface, and lowering the coolant's inlet temperature, ideally through natural subsurface cooling.

It is important to emphasize that the optimal configuration is highly dependent on the local environmental conditions, including ambient temperatures, solar irradiation, and soil thermal behavior. Nevertheless, based on the results presented in Figure 17, a configuration comprising 10 to 16 pipes, combined with a coolant temperature of 10 °C or lower, demonstrates a significant reduction in peak panel temperatures, especially in hotter environments, offering a balanced and practical approach for real-world deployment.

4 Discussion and Conclusion

This study evaluated the performance of an integrated PV/T cooling system using both experimental measurements and computational modeling. The experimental setup enabled the assessment of the active cooling system and allowed for comparisons with real-world configurations featuring no cooling or passive cooling. Additionally, a computational model was developed to represent an ideal case, providing the base for evaluating system performance under ideal condition and possible optimizations.

Based on the analysis of the experimental layout in Finnfoam yard, the performance of the PV system showed an improvement in power output for 2024 compared to 2023, but not in comparison to 2022. However, when analyzing performance by individual groups and normalizing the results, as Group B was equipped with the cooling system, underperformed relative to Groups A and C. This is most likely due to poor thermal contact between the coolant pipes and the panel surface, rather than a design failure. Favorable weather conditions in 2024 may also explain the overall performance increase, independent of the cooling system.

Despite limited experimental gains, the computational model confirmed that the cooling system is effective under ideal conditions, showing a significant reduction in panel temperature when the system is properly configured. This correlates with improved panel efficiency, as lower temperatures lead to higher photovoltaic performance.

The effectiveness of the cooling system improves in hotter environments, making it more suitable for regions with both high-irradiation and high-temperature. Under identical configurations (same number of pipe passes and coolant temperature), the temperature decrease achieved in hotter regions (e.g., southern Spain) was greater than in colder climates (e.g., southwest Finland). This makes hot regions more suitable candidates for system deployment. However, the profiles are an average representation of ambient conditions and real-life conditions may lead higher thermal peaks than the represented in the model. Achieving optimal operating temperatures (around 25°C) in hot climates requires either more aggressive cooling strategies or system design changes.

The computational model is highly adaptable and can be configured to simulate performance across various geographic locations. It not only accounts for the seasonal variation of the Sun's path, but also integrates localized irradiation and ambient temperature profiles to reflect real-world environmental conditions. Additionally, the model supports flexible system geometry, allowing users to add or remove solar panels, modify the piping layout, and adjust critical parameters such as soil temperature gradients and coolant temperature. This versatility enables detailed virtual studies to optimize system design and evaluate its feasibility for deployment in specific locations.

When adapting the system to a different geographical location, the following must be considered: Optimal design depends heavily on local environmental conditions such as solar radiation, ambient temperature, and wind speed; the computational model does not currently account for wind, rain, diffuse radiation, or dust deposition—all of which can affect real-life performance; in desert regions, dust storms and deposition, particularly during the Harmattan season in areas like the Sahara, may significantly impact effectiveness, and if the system relies on subsurface cooling, it is essential to assess or measure local soil temperature profiles to determine feasibility. In general, based on solar profiles, pump operation is recommended between 07:00 and 18:00 for optimal thermal control.

In real-world setups, lower-than-expected performance may result from poor thermal contact between the panels and the cooling pipes. The application of thermal paste could substantially improve heat transfer, but would require a permanent bond between components.

Based on ADRASE [32] solar radiation data, the southern mainland coast of Spain presents an excellent location for implementation. For this region, based on the simulation results, it is suggested a configuration of 10–18 pipe passes and maintaining coolant temperatures at or below 10 °C to yield the best results during the hottest season. If maintaining such low coolant temperatures is not feasible, the model can be adjusted to explore alternative configurations (e.g., more passes, different pipe materials, or contact enhancements).

The model always accounts with a virtually inexhaustible thermal source, as the coolant is always supplied at the same temperature. Real-life sources may vary the supplied temperature according to the reservoir used.

This study demonstrated that the active cooling designed by Finnfoam can significantly enhance thermal regulation and improve overall panel performance, especially in hot climates with high solar irradiation. By combining experimental validation with computational modeling, the study highlighted the limitations of the PV/T system and emphasized the value of location-specific optimization. The calibrated thermal model proved effective in predicting panel behavior under varying environmental conditions, reinforcing the importance of adaptable designs for maximizing efficiency in diverse geographic settings.

References

[1] P. Dwivedi, K. Sudhakar, A. Soni, E. Solomin, and I. Kirpichnikova, "Advanced cooling techniques of p.v. modules: A state of art," *Case Studies in Thermal Engineering*, vol. 21, p. 100 674, 2020, ISSN: 2214-157X. DOI: `https://doi.org/10.1016/j.csite.2020.100674`. [Online]. Available: `https://www.sciencedirect.com/science/article/pii/S2214157X19305416`.

[2] H. Ritchie, P. Rosado, and M. Roser, "Energy production and consumption," *Our World in Data*, 2020. [Online]. Available: `https://ourworldindata.org/energy-production-consumption`.

[3] C. S. Kumar. (Sep. 2016). "We could power the entire world by harnessing solar energy from 1% of the sahara," [Online]. Available: `https://www.forbes.com/sites/quora/2016/09/22/we-could-power-the-entire-world-by-harnessing-solar-energy-from-1-of-the-sahara/` (visited on 02/20/2025).

[4] K. Kurokawa, *Energy from the desert : feasibility of very large scale photovoltaic power generation (VLS-PV) systems (1st ed.).* Earthscan, 2013. DOI: `10.4324/9781315074443`.

[5] P. H. Chen, W.-S. Chen, C.-H. Lee, and J.-Y. Wu, "Comprehensive review of crystalline silicon solar panel recycling: From historical context to advanced techniques," *Sustainability*, vol. 16, p. 60, Dec. 2023. DOI: `10.3390/su16010060`.

[6] B. Zaidi and B. Zaidi, *Solar panels and photovoltaic materials*, eng. London, England: IntechOpen, 2018, ISBN: 9781838816476.

[7] S. J. Fonash, *Solar Cell Device Physics.* Elsevier Science & Technology, 2010.

[8] B. R. Sutherland, "Solar materials find their band gap," *Joule*, vol. 4, no. 5, pp. 984–985, 2020, ISSN: 2542-4351. DOI: `https://doi.org/10.1016/j.joule.2020.05.001`. [Online]. Available: `https://www.sciencedirect.com/science/article/pii/S2542435120301847`.

[9] M. S. Khan, V. Hegde, and G. Shankar, "Effect of temperature on performance of solar panels- analysis," pp. 109–113, 2017. DOI: `10.1109/CTCEEC.2017.8455109`.

[10] S. Dubey, J. N. Sarvaiya, and B. Seshadri, "Temperature dependent photovoltaic (pv) efficiency and its effect on pv production in the world – a review," *Energy Procedia*, vol. 33, pp. 311–321, 2013, PV Asia Pacific Conference 2012, ISSN: 1876-6102. DOI: `https://doi.org/10.1016/j.egypro.2013.05.072`. [Online]. Available: `https://www.sciencedirect.com/science/article/pii/S1876610213000829`.

[11] Y. Zhao, S. Gong, C. Zhang, M. Ge, and L. Xie, "Performance analysis of a solar photovoltaic power generation system with spray cooling," *Case Studies in Thermal Engineering*, vol. 29, p. 101 723, 2022, ISSN: 2214-157X. DOI: `https://doi.org/10.1016/j.csite.2021.101723`. [Online]. Available: `https://www.sciencedirect.com/science/article/pii/S2214157X21008868`.

[12] D. Cotfas, P. Cotfas, and O. Machidon, "Study of temperature coefficients for parameters of photovoltaic cells," *International Journal of Photoenergy*, vol. 2018, pp. 1–12, Apr. 2018. DOI: `10.1155/2018/5945602`.

[13] B. R. Paudyal and A. G. Imenes, "Investigation of temperature coefficients of pv modules through field measured data," *Solar Energy*, vol. 224, pp. 425–439, 2021, ISSN: 0038-092X. DOI: `https://doi.org/10.1016/j.solener.2021.06.013`. [Online]. Available: `https://www.sciencedirect.com/science/article/pii/S0038092X21004837`.

[14] M. Shehadi, "Optimizing solar cooling systems," eng, *Case studies in thermal engineering*, vol. 21, pp. 100 663–, 2020, ISSN: 2214-157X.

[15] V. Ramasamy, J. Zuboy, M. Woodhouse, E. O'Shaughnessy, D. Feldman, J. Desai, A. Walker, R. Margolis, and P. Basore, "U.s. solar photovoltaic system and energy storage cost benchmarks, with minimum sustainable price analysis: Q1 2023," National Renewable Energy Laboratory, Golden, CO, Tech. Rep. NREL/TP-7A40-87303, 2023. [Online]. Available: `https://www.nrel.gov/docs/fy23osti/87303.pdf` (visited on 06/18/2025).

[16] S.-Y. Wu, Q.-L. Zhang, L. Xiao, and F.-H. Guo, "A heat pipe photovoltaic/thermal (pv/t) hybrid system and its performance evaluation," *Energy and Buildings*, vol. 43, no. 12, pp. 3558–3567, 2011, ISSN: 0378-7788. DOI: `https://doi.org/10.1016/j.enbuild.2011.09.017`. [Online]. Available: `https://www.sciencedirect.com/science/article/pii/S0378778811004051`.

[17] K. Stewart. (). "Propylene glycol," [Online]. Available: `https://www.britannica.com/science/propylene-glycol`.

[18] H. KOFFI, V. Kakane, A. Kuditcher, A. Hughes, M. Adeleye, and J. Amuzu, "Seasonal variations in the operating temperature of silicon solar panels in southern ghana," *African Journal of Science, Technology, Innovation and Development*, vol. 7, pp. 1–6, Jul. 2015. DOI: `10.1080/20421338.2015.1038006`.

[19] W. Commons, *Blank Map of the World*, Wikimedia Commons, Accessed: 2025-07-28. Original file is an SVG vector graphic., 2011. [Online]. Available: `https://commons.wikimedia.org/wiki/File:BlankMap-World.svg`.

[20] The Engineering ToolBox. (2003). "Thermal conductivity of some common materials and gases," [Online]. Available: `https://www.engineeringtoolbox.com/thermal-conductivity-d_429.html` (visited on 06/21/2025).

[21] ——, (2003). "Ducts - surface roughness," [Online]. Available: `https://www.engineeringtoolbox.com/surface-roughness-ventilation-ducts-d_209.html` (visited on 06/21/2025).

[22] K. Stewart. (). "Photovoltaic geographical information system," [Online]. Available: `https://re.jrc.ec.europa.eu/pvg_tools/en/.`.

[23] W. Z. Leow, Y. M. Irwan, I. Safwati, M. Irwanto, A. R. Amelia, Z. Syafiqah, M. I. Fahmi, and N. Rosle, "Simulation study on photovoltaic panel temperature under different solar radiation using computational fluid dynamic method," *Journal of Physics: Conference Series*, vol. 1432, no. 1, p. 012 052, Jan. 2020. DOI: `10.1088/1742-6596/1432/1/012052`. [Online]. Available: `https://dx.doi.org/10.1088/1742-6596/1432/1/012052`.

[24] The Engineering ToolBox, *Ethylene glycol - density and specific weight*, Accessed: 2025-05-13, 2025. [Online]. Available: `https://www.engineeringtoolbox.com/ethylene-glycol-d_146.html`.

[25] M. Hashmi, “Plastics and elastomers,” in *Comprehensive Materials Processing*, S. Hashmi, Ed., Elsevier, 2014, ch. 2, pp. 21–51. DOI: `10.1016/B978-0-443-18786-5.00002-0`. [Online]. Available: `https://www.sciencedirect.com/science/article/pii/B9780443187865000020`.

[26] Á. Fernández-Solas, L. Micheli, F. Almonacid, and E. F. Fernández, “Optical degradation impact on the spectral performance of photovoltaic technology,” *Renewable and Sustainable Energy Reviews*, vol. 141, p. 110 782, 2021, ISSN: 1364-0321. DOI: `https://doi.org/10.1016/j.rser.2021.110782`. [Online]. Available: `https://www.sciencedirect.com/science/article/pii/S1364032121000770`.

[27] J. Nelson, *The Physics of Solar Cells: Photons In, Electrons Out.* Imperial College Press, 2003, Section 7.3 for the notion that direct band-to-band absorption in silicon cells drops post 1.1, ISBN: 1-86094-340-3.

[28] C. J. Chen, *Physics of solar energy*, eng, 1st ed. Hoboken, N.J: John Wiley Sons, 2011, ISBN: 9786613246516.

[29] N. R. E. L. (NREL). (). “Reference air mass 1.5 spectra,” National Renewable Energy Laboratory, [Online]. Available: `https://www.nrel.gov/grid/solar-resource/spectra-am1.5` (visited on 06/21/2025).

[30] U.S. Department of Energy, “Climate calculations,” in *EnergyPlus Engineering Reference.* 2020, Documentation hosted by Big Ladder Software. [Online]. Available: `https://bigladdersoftware.com/epx/docs/9-3/engineering-reference/climate-calculations.html` (visited on 06/21/2025).

[31] M. Khalis, R. Masrour, G. Khrypunov, M. Kirichenko, D. Kudiy, and M. Zazoui, “Effects of temperature and concentration mono and polycrystalline silicon solar cells: Extraction parameters,” *Journal of Physics: Conference Series*, vol. 758, 2016, ISSN: 1742-6588. DOI: `10.1088/1742-6596/758/1/012001`.

[32] ADRASE, *Mapa zona península*, `https://www.adrase.es/acceso-a-los-mapas/mapa-zona-peninsula.html`, Accessed: 2025-05-20, n.d.

[33] T. Huld, R. Müller, and A. Gambardella, "A new solar radiation database for estimating PV performance in Europe and Africa," *Solar Energy*, vol. 86, no. 6, pp. 1803–1815, 2012. DOI: `10.1016/j.solener.2012.03.006`.

[34] T. Rahman, A. A. Mansur, M. S. Hossain Lipu, M. Rahman, R. H. Ashique, M. Abou Houran, R. Madurai Elavarasan, and E. Hossain, "Investigation of degradation of solar photovoltaics: A review of aging factors, impacts, and future directions toward sustainable energy management," *Energies*, vol. 16, p. 3706, Apr. 2023. DOI: `10.3390/en16093706`.

[35] P. Pipe and F. Association, *Pvc*, Accessed: 2025-06-22, 2025. [Online]. Available: `https://www.ppfahome.org/page/pvc`.

[36] Puuilo, *Yorkshire kupariputki kova 15x13 2,5m*, Accessed: 2025-06-22, 2025. [Online]. Available: `https://www.puuilo.fi/yorkshire-kupariputki-kova-15x13-2-5m`.

[37] ——, *Wehosani pex-käyttövesiputki pn10 15mm 1m*, Accessed: 2025-06-22, 2025. [Online]. Available: `https://www.puuilo.fi/wehosani-pex-kayttovesiputki-pn10-15mm-1m`.

[38] IKH, *Muoviletku pvc kirkas 9x12mm fit013*, Accessed: 2025-06-22, 2025. [Online]. Available: `https://www.ikh.fi/fi/muoviletku-pvc-kirkas-9x12mm-fit013`.

[39] K-Rauta, *Kupariputki cupori 15mm suora kova*, Accessed: 2025-06-22, 2025. [Online]. Available: `https://www.k-rauta.fi/tuote/kupariputki-cupori-15mm-suora-kova/6415815810142`.

[40] ——, *Pex käyttövesi-/lämpöjohtoputki 15x2.5 pn10 120m*, Accessed: 2025-06-22, 2025. [Online]. Available: `https://www.k-rauta.fi/tuote/pex-kayttovesilampojohtoputki-15x25-pn10-120m/4044599030174`.

[41] ——, *Muoviletku toppbright 12/25m kirkas*, Accessed: 2025-06-22, 2025. [Online]. Available: `https://www.k-rauta.fi/tuote/muoviletku-toppbright-1225m-kirkas/6416773312143`.

[42] Biltema, *Kupariputki 15 mm x 2 m*, Accessed: 2025-06-22, 2025. [Online]. Available: `https://www.biltema.fi/rakentaminen/lvi/vesijarjestelmat-ja-saniteetti/kupariputket/kupariputket/kupariputki-15-mm-x-2-m-2000058873`.

[43] ——, *Pex-putki, 15 x 2,5 mm x 25 m*, Accessed: 2025-06-22, 2025. [Online]. Available: `https://www.biltema.fi/rakentaminen/lvi/vesijarjestelmat-ja-saniteetti/pex-letkut-ja-liittimet/pex-letkut/pex-putki-15-x-25-mm-x-25-m-2000058748`.

[44] ——, *Pvc-letku 5 m x 12 mm*, Accessed: 2025-06-22, 2025. [Online]. Available: `https://www.biltema.fi/veneily/veneen-lvi-jarjestelma/letkut/pvc-muoviletkut/pvc-letku-5-m-x-12-mm-2000060033`.

[45] Talotuote, *Kupariputki 15mm suora kova 5m*, Accessed: 2025-06-22, 2025. [Online]. Available: `https://talotuote.fi/p41573/kupariputki-15mm-suora-kova-5m`.

[46] Bauhaus, *Pex-käyttövesiputki wehosani 15 x 2,5 mm*, Accessed: 2025-06-22, 2025. [Online]. Available: `https://www.bauhaus.fi/pex-kayttovesiputki-wehosani-15-x-2-5-mm.html`.

[47] IKH, *Pvc-letku 12 mm*, Accessed: 2025-06-22, 2025. [Online]. Available: `https://www.bauhaus.fi/pvc-letku-12-mm.html`.

A Validation profiles

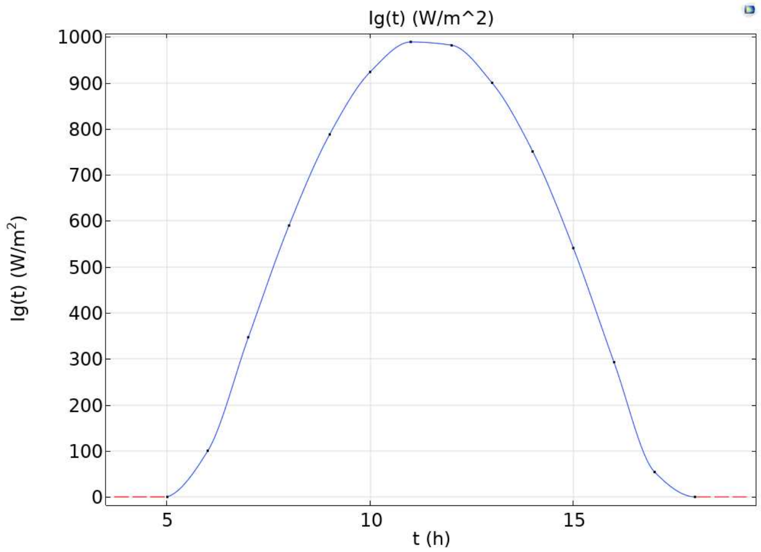

(a)

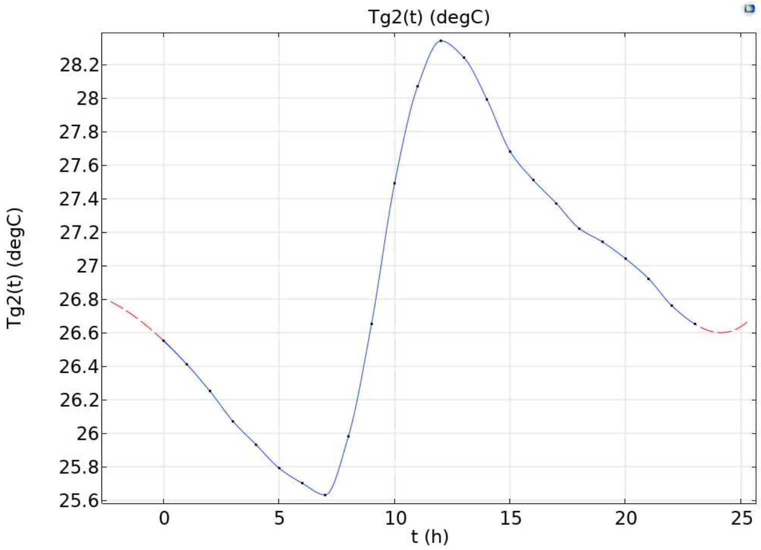

(b)

Figure 18: Accra, Ghana (a) solar irradiation and (b)temperature profile for Harmattan season sourced form PVGIS [22].

B Study cases

Here it is shown the graphs used to adjust the temperature curve for each study case.

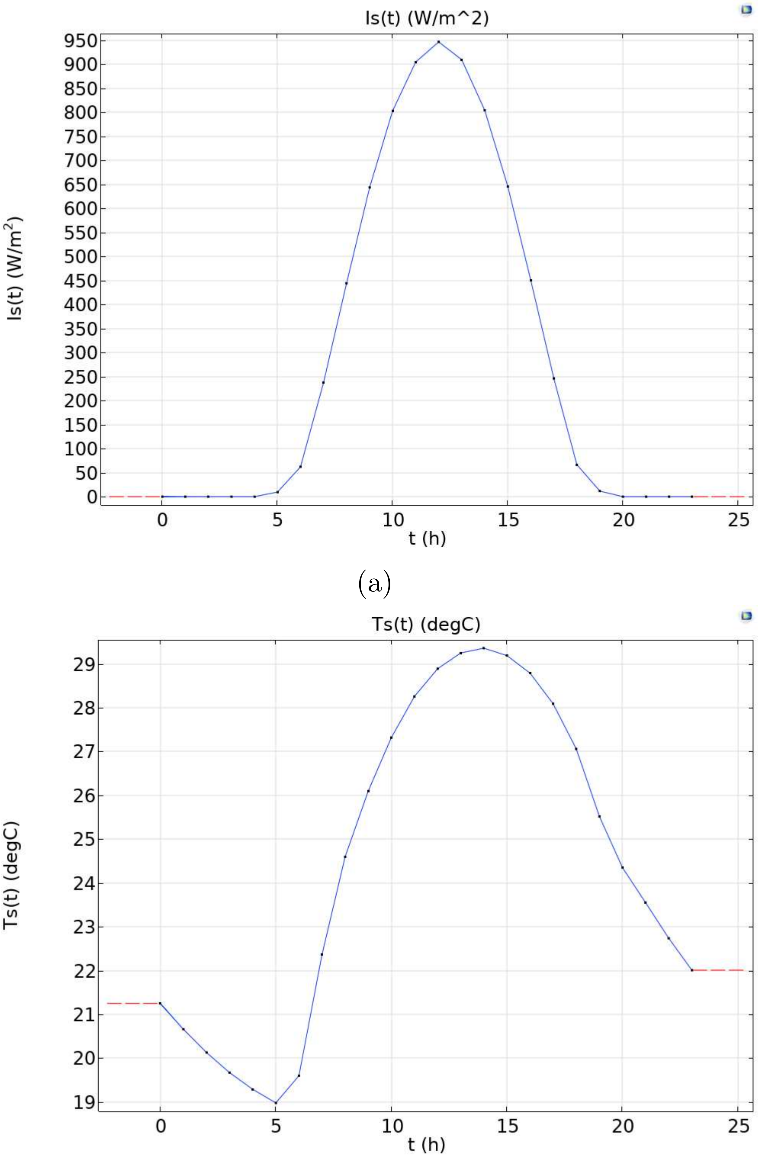

(a)

(b)

Figure 19: Tabernas Desert, Spain July (a) solar irradiation and (b)temperature profile sourced form PVGIS [22].

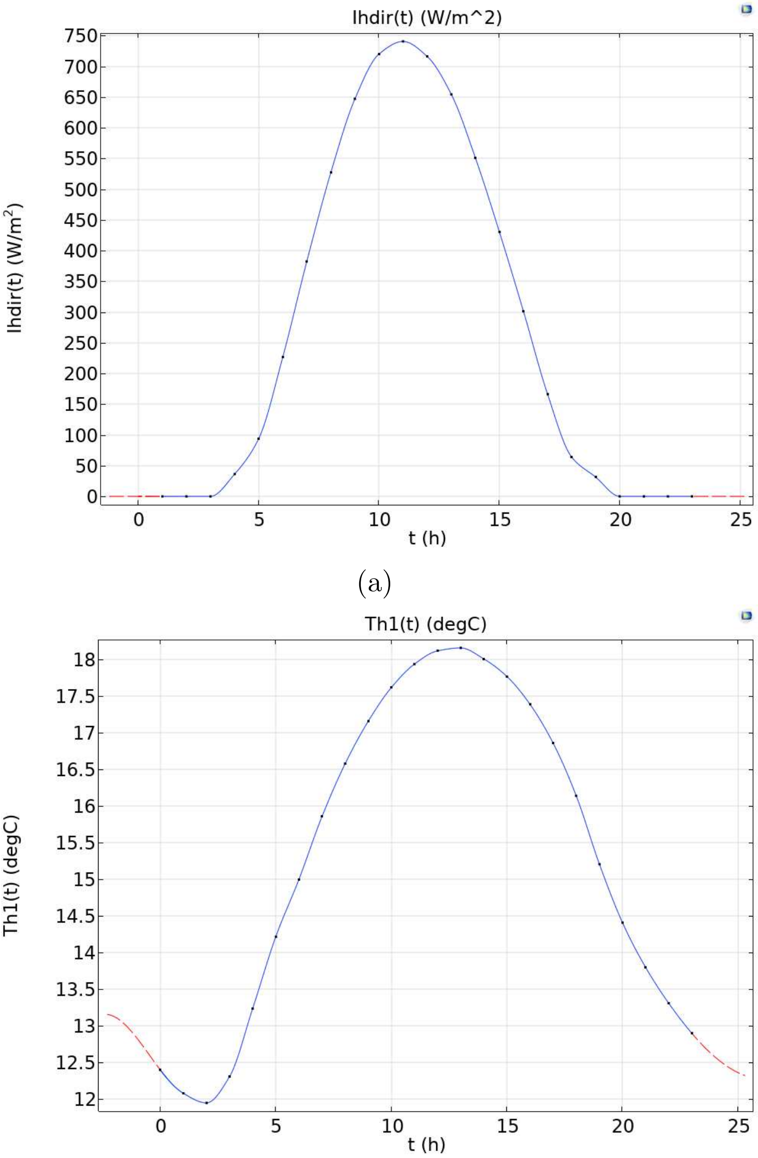

(a)

(b)

Figure 20: Helsinki, Finland June (a) solar irradiation and (b)temperature profile sourced form PVGIS [22]..

C Material Assessment

Table 9: Prices of three different piping materials and inner diameters according to different suppliers in Finland.

Copper [$\phi = 15mm$]		**PEX [$\phi = 12mm$]**		**PVC [$\phi = 15mm$]**	
Company	**Euro/m**	**Company**	**Euro/m**	**Company**	**Euro/m**
Puuilo [36]	10.12	Puuilo [37]	2.79	IKH [38]	0.70
K-Rauta [39]	13.95	K-Rauta [40]	2.99	K-Rauta [41]	2.76
Biltema [42]	10.00	Biltema [43]	2.00	Biltema [44]	0.91
Talotuote [45]	10.52	Bauhaus [46]	2.80	Bauhaus [47]	2.20
Average	**11.15**		**2.65**		**1.64**